Two-Stage Solid-Phase Transition of Cubic Ice to Hexagonal Ice: Structural Origin and Kinetics

Shu-hui Guan,[†,‡] Cheng Shang,*,[‡] Si-Da Huang,[‡] and Zhi-Pan Liu*,[‡]

†Shanghai Academy of Agricultural Sciences, Shanghai 201403, China

‡Collaborative Innovation Center of Chemistry for Energy Material, Shanghai Key Laboratory of Molecular Catalysis and Innovative Materials, Key Laboratory of Computational Physical Science, Department of Chemistry, Fudan University, Shanghai 200433, China

Ⓢ *Supporting Information*

ABSTRACT: Two most known ice phases, cubic (Ic) and hexagonal ice (Ih), are observed to coexist over a surprisingly broad low temperature range (150−240 K) in ice particles, the origin of which, despite great efforts devoted to revealing the ice microstructures in experiment, remains largely unknown. Here by combining global sampling with machine learning potential, the stochastic surface walking-neural network method, we reveal all key metastable intermediates during the Ic-to-Ih phase transition, which are basically low-energy structural defects in ice, including vacancies, heterophase junctions, and stacking faults. This leads to the first identification of the lowest energy pathways from ice Ic to Ih, where the presence of vacancy defects in ice allows the transformation kinetically by initiating a fast Ih nucleation. The subsequent migration of a vacancy, with a barrier of 48 kJ/mol, turns out to be the rate-determining step in Ih phase growth, rationalizing the unexpected prevalence of anisotropic stacking faults in low-temperature ice particles. This vacancy-controlled kinetics in Ih formation arises from the flexibility of the local geometry of a weaker H-bonding environment around the vacancy, which suggests that the frustrated material with a complex energy landscape may seek an unusual phase transition pathway with the help of a low level of heterogeneity.
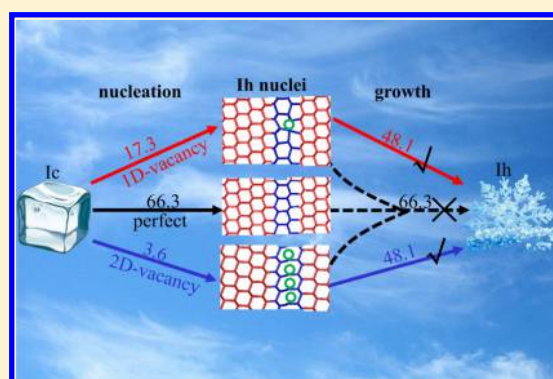
1. INTRODUCTION

Ice plays a basic role in the evolution of the universe.[1−3] The hexagonal phase, ice Ih, is the most stable phase upon freezing at ambient pressure or below, whereas the cubic phase, ice Ic, has recently been shown to be a key metastable phase (35 J/mol less stable at ∼170 K[4,5]) that crystalizes first from water and transforms irreversibly into ice Ih[2−4,6] above ∼150 K (Figure 1). This crystal phase transition, being sensitive to ice microstructures, is central to natural phenomena ranging from cloud formation,[7] to the dehydration of materials,[8] and to ozone depletion.[9] Considerable efforts are therefore devoted to identifying ice defects (e.g., vacancies, heterophase junctions (**HJ**), and stacking faults) and understanding this transition kinetics. However, the atomic structure of ice defects remains largely elusive, which leads to a great difficulty in understanding their roles in phase transition kinetics and consequently some key properties of ice, such as roughness and environmental humidity.[8−10]

It is known that an ice Ih crystal has a rhombic unit cell with four H_2O molecules, and ice Ic has a cubic unit cell with eight molecules,[1] as shown in Figure 1. For both crystals, the water molecules form layers consisting of six-membered puckered rings. Since the 1960s, extensive experimental studies[7,11−16] (e.g., using X-ray diffraction,[11] differential thermal analysis,[15]
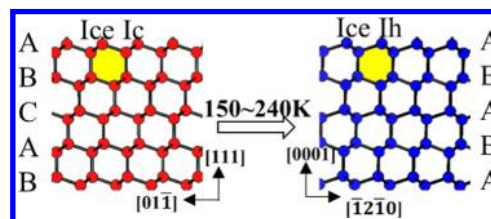

Figure 1. Perfect hexagonal and cubic ice crystals in ball-and-stick representation. Only the oxygen atoms are shown, which are interconnected by H-bondings, as dictated by the Bernal−Fowler rule. In ice Ih, each layer is a mirror image of the previous layer, whereas for ice Ic each successive layer is shifted a distance equal to half the diameter of the six-membered ring. As a result, ice Ih can be considered as a regular [ABABAB]∞ stacking along the hexagonal c-axis ([0001]h), and ideal ice Ic forms a cubic [ABCABC]∞ stacking along a cubic [111]c direction.

calorimetric study,[13] and in situ neutron powder diffraction[16]) have shown that the Ic-to-Ih transition occurs mainly at ∼190−205 K with small but detectable events starting as early

as $\approx$150 K[14] and ending up to 240 K.[15] The reaction is sensitive to the preparation conditions, as reflected by the varied kinetics reported from different experiments (minutes to days below 200 K[8]). Consistently, the kinetic analyses by Sugisaki et al.[13] derived two distinct activation energies, i.e., 21.3 kJ/mol at 160 K and 44.7 kJ/mol at 210 K. This puzzling two-step transition was suspected to be associated with the intrinsic defects in ice,[16,17] and such structural defects in ice may originate from two sources. First, the initial Ic phase is known to be imperfect, as shown by a number of experiments;[10] second, some additional defects,[16,18,19] in particular anisotropic stacking faults, may further evolve in the phase transition that hinders the Ih growth from the Ic matrix.[17]

Identifying these intrinsic defects in ice is, however, technically difficult in experiment, not only because the high spatial resolution required is beyond current instrument capabilities[20−22] but also because of the fact that the defects' concentration is low and prone to thermal fluctuations. On the other hand, ice as a typical molecular crystal is long known as a "frustrated system" with numerous configurations,[6] as seen from molecular simulations. As summarized by Malkin et al.,[19] fundamental challenges are faced nowadays to capture the structure of ice nucleus from theory: the accuracy of the potential energy surface (PES), the rare nature of nucleation events, and the structure discrimination of different ice/water forms. For these reasons, to date, both the microstructure and the Ic-to-Ih transition pathway have been largely unknown.

In this work, using a recently developed SSW-NN method,[23] i.e., the stochastic surface walking (SSW) global sampling with the neural network (NN) potential auto-trained from first-principles dataset, we explore for the first time the global PES of ice and resolve the transformation kinetics from ice Ic to Ih. A group of key low-energy structural defects in ice are characterized, and their roles in the Ic-to-Ih transition are identified. With all kinetic data, we propose the mechanism of ice Ih formation, where the long-standing puzzles on the broad range of transition temperatures and the presence of anisotropic stacking faults in ice are now clarified at the atomic level.

2. METHODS AND CALCULATION DETAILS

All calculations, including the exploration of the global phase space of ice crystals and the reaction sampling (RS), were carried out based on the NN potential that are auto-trained from first-principles global PES data. The NN potential generation utilizes our previously developed SSW-NN method that follows a "global-to-global" recipe of constructing a global and accurate NN PES for materials. The NN potential significantly speeds up PES sampling by more than 4 orders of magnitude with comparable accuracy to the first-principles calculations.[23] With the SSW-NN approach, we are able to sample the highly complex PES of ice extensively and unbiasedly, leading to the identification of all transient microstructures in ice, ranging from metastable crystal forms to heterophase junctions (**HJ**) and to vacancy defects (**Def**).

2.1. SSW Global Search and Pathway Sampling. The SSW method is first utilized to explore the PES of the ice phase space, which takes advantage of the global optimization functionality of the SSW method[24−26] (SSW methodology is detailed in our previous work). The SSW based reaction sampling (SSW-RS) is then utilized to sample the solid reaction pathways, exhaustively and unbiasedly, from which we

obtain the crystal-to-crystal solid-phase transition pathway between ice Ic and ice Ih.

For clarity, here we outline the SSW-RS method briefly. The SSW-RS is based on the SSW global optimization method and is targeted for finding one-step or short-pathway reactions in an automated way. The SSW method is able to explore complex PES to identify unexpected new structures and, in the meantime, to collect the reaction pathways leading to them. For solid-phase transitions, this is to identify the one-to-one correspondence for the lattice ($L(e_1,e_2,e_3)$, e_i being the lattice vector) and atom (q_i, i = 1, ..., 3N, N is the number of atoms in the cell) from one crystal phase (the initial state, IS) to another (the final state, FS), which constitutes the reaction coordinates of the reaction, i.e., $Q_{IS}(L,q) \rightarrow Q_{FS}(L,q)$. In one SSW pathway sampling simulation, we need to collect as many such IS/FS pairs (typically a few hundreds) as possible to ensure the identification of the best reaction coordinate, the one corresponding to the lowest energy pathway. With such a pair of reaction coordinates, $Q_{IS}(L,q)$ and $Q_{FS}(L,q)$, it is then possible to utilize the variable-cell double-ended surface walking (VC-DESW[27]) method to identify the reaction transition state (TS) and the minimum energy pathway.

In our implementation, the SSW pathway sampling is fully automated and divided into three stages in simulation, namely, (i) pathway collection via extensive SSW global search; (ii) pathway screening via fast DESW pathway building; and (iii) lowest energy pathway determination via DESW TS search. The first stage is the most important and also the most time-consuming, which generates all likely pairs of the generalized reaction coordinates, linking different crystal phases. For example, for the ice Ic-to-Ih phase transition mediated by a particular heterophase junction, our SSW pathway sampling starts from this heterophase junction (e.g., **HJ-1** in Table 1),

Table 1. Structural Properties and Energetics for Four Lowest Energy Heterophase Junctions[a]

name	interface	OR	ΔS (%)	γ	E_a
HJ-1	$(111)_c//(0001)_h$	OR-1	−0.5	0.03	66.3
HJ-2	$(\bar{2}11)_c//(01\bar{1}0)_h$	OR-1	1.1	22.5	80.8
HJ-3	$(01\bar{2})_c//(1\bar{2}10)_h$	OR-1	0.3	27.1	151.9
HJ-4	$(001)_c//(0001)_h$	OR-2	−7.8	57.4	201.9

[a]Listed data include the interface planes, the crystallographic orientation relationship (OR), the area misfit between connecting phases at the interface (ΔS, with respect to Ic), the interfacial energy (γ, kJ/(mol Å^{-2})), and the reaction barrier (E_a, kJ/mol) for the heterogeneous pathway for the Ic-to-Ih transition mediated by the corresponding junction.

defined as IS, and then explores exhaustively the likely phases nearby (>2000 minima), defined as FS. After collecting a significant number of IS/FS pairs, i.e., >200 pairs, we utilize VC-DESW to locate the TS explicitly between IS and FS, based on which the low-energy pathways connecting Ic and Ih are determined by sorting the computed barriers (also see the Supporting Information (SI)).

2.2. Ice NN Potential. The SSW global optimization plays the central role in SSW-NN for both generating the global dataset used in NN potential fitting and exploring global PES to identify unknown phases/pathways. In this work, the final training dataset for the NN potential of ice contains 58825 distinct structures from first-principles density functional theory (DFT) calculations that are obtained iteratively by
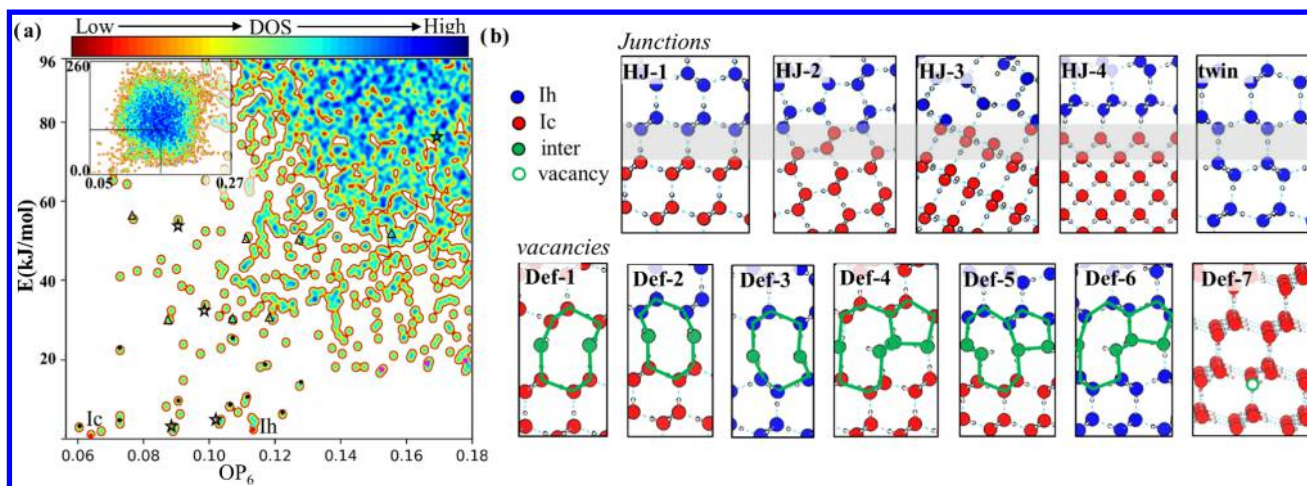
Figure 2. (a) Two-dimensional global PES for low-energy ice structures using the OP$_6$−E contour plot, as enlarged from the same plot (the inset) using the total dataset from the SSW-NN simulation. OP$_6$: the structure order parameter with $L = 6$ (only considering the O sublattice). The energy of Ic is set as zero. (b) The lowest energy defective structures, including heterophase junctions (**HJ**), faults (upper panel), and vacancy defects (**Def**) (lower panel). These defective structures are also labeled in (a), and their coordinates (OP$_6$, E) are as follows: **HJ-1**(0.087,0.96); **HJ-2**(0.097,33.42); **HJ-3**(0.090,56.59); **HJ-4**(0.168,75.92); **twin**(0.113,3.0); **Def-1**(0.088,30.3); **Def-2**(0.107,30.2); **Def-3**(0.119,30.3); **Def-4**(0.126,50.4); **Def-5**(0.113,50.8); **Def-6**(0.157,54.2); **Def-7**(0.0762,58.2).

self-learning the global PES data. In the process, more than 10^6 minima are visited using SSW global optimization of water clusters/solids. All first-principles calculations were performed using the plane-wave DFT code, VASP,[28] with van der Waals-corrected generalized gradient approximation−Perdew−Burke−Ernzerhof functional (PBE-D3)[27,29] (see the SI for other details).

Our theoretical procedure to set up the structural descriptors and network size of the NN potential are discussed in detail in the SI, where we verify that the structure descriptor set is enough, and the network size is optimal to achieve high accuracy. After training the network on the global dataset, we obtain the first ice global NN PES with root-mean-square error (RMSE) values for energy, force, and stress being 2.1 meV/atom, RMS 0.08 eV/Å, and 1.07 GPa (the performance for the test dataset achieves a similar accuracy and the energy-resolved RMSE for the test dataset is shown in Figure S9 in the SI). The overall accuracy is quite standard for global NN PES considering that the energy of the structures in the dataset spans a large window up to 1.4 eV/atom energy difference.

We have examined the accuracy of the NN PES for the representative crystal ice structures and benchmarked them against DFT calculations, as listed in Tables S2−S5. These structures were fully optimized using NN until the maximal force component is below 0.01 eV/Å and the stress is below 0.01 GPa, and then refined using DFT for comparison. As shown, the energy RMS error is only 0.6 meV/atom for typical low-energy minima, and the error in reaction barriers is below 0.8 meV/atom for phase transition pathways. Such an accuracy is sufficient for global structure and pathway search to identify the low-energy candidates.

3. RESULTS

Our investigation starts by exploring the ice global PES using SSW, more than 50 000 minima visited for the 36-atom and 45-atom supercell systems (other larger unit cells up to 177 atoms are also examined until no new local structure patterns are discovered). After removing the same isomers, we finally obtain 6161 distinct minima, including crystals and amorphous structures. To visualize the structures, we project them on a two-dimensional (2D) structure−energy contour plot in Figure 2a. The structure fingerprint (x-axis), the distance-weighted Steinhart order parameter with degree $L = 6$ (OP$_6$), is utilized (also see SI) in the projection, which is found to be sensitive to distinguish different ice forms.

3.1. Global PES and Key Structure Motifs. Figure 2a shows that there are a substantially large number (475) of distinct crystal minima below ∼60 kJ/mol. Above 60 kJ/mol, the amorphous structures dominate with a large density of states. The low-energy minima contain single, mixed-phase crystalline structures and also different crystal defects, from which new crystal phases and energetically favored defects can be gleaned. The two common ice phases, Ic and Ih, at ambient pressure, as marked by red dots, locate at the bottom of Figure 2a. The other less stable crystalline phases with high symmetry are highlighted by pink dots, including the known structures with space group #138,[30] #139,[31] #74[32] and also the newly found crystal structures with space group #62, #71 (all summarized in the SI). As they are not the focus of this work, here we merely mention that these new metastable phases may play a significant role in water crystallization as their local structural motifs can be closer to liquid water compared to the Ic and Ih phases, as reflected by the OP$_6$. Tanaka et al.[30] have pointed out that the #138 phase (also named ice-0) might be a precursor phase in water crystallization from molecular dynamics simulations.

Now we focus on the ice defects that could be critical to the Ic-to-Ih phase transition. In total, four low-energy metastable heterophase junctions (as indicated by star symbols in Figure 2a), seven common vacancy defects (triangle symbols), and many twins/stacking faults (black dots) can be screened out from Figure 2a. They can further be distinguished according to the interface type, crystallographic orientation relationships (OR), and the structural characteristics near the vacancies.

The four heterophase junctions, as characterized by the interface structure (shown at the top of Figure 2b), named **HJ-1** to **HJ-4**, belong to two distinct ORs, **OR-1** and **OR-2**. **HJ-1** corresponds to **OR-1**: $(111)_c//(0001)_h$; $[1\bar{1}0]_c//[2\bar{1}\bar{1}0]_h$,
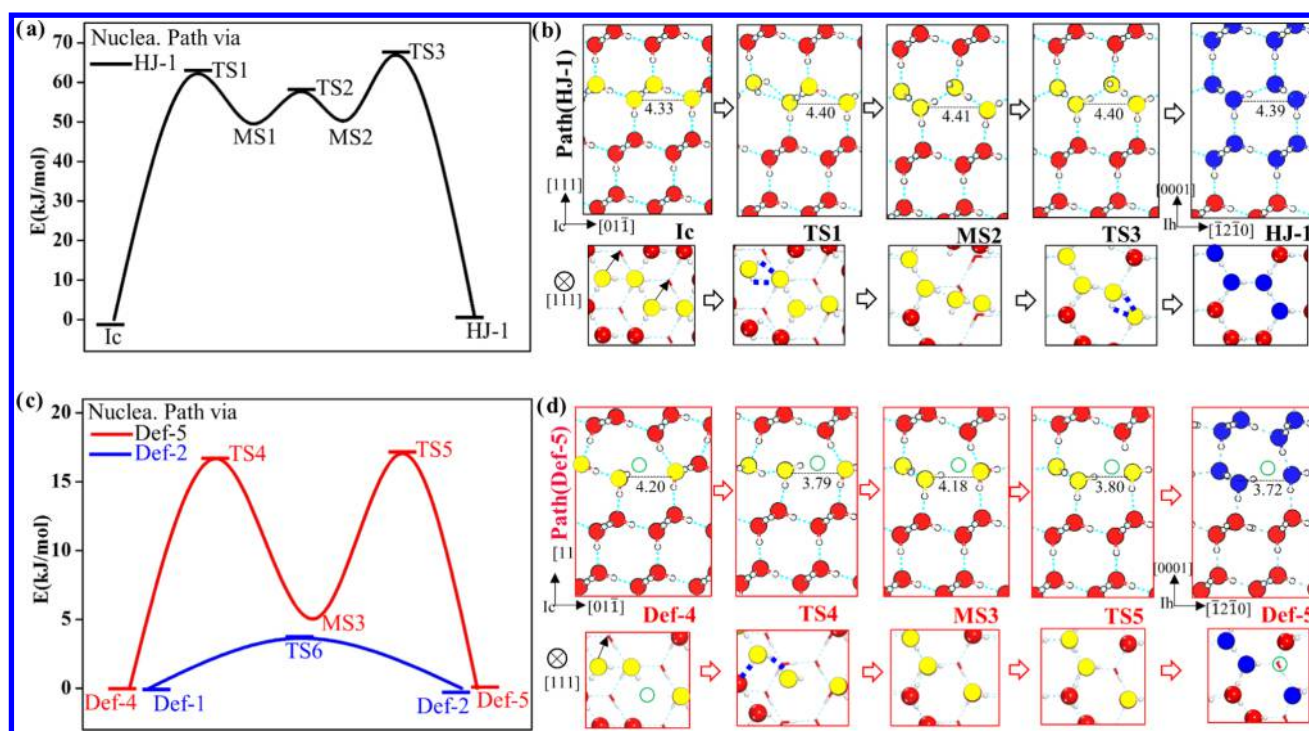
Figure 3. Potential energy profile for Ih nucleation reaction pathways mediated by vacancy-free heterophase junction **HJ-1** (a) and by vacancies (c), i.e., from **Def-4** to **Def-5** and from **Def-1** to **Def-2**. The corresponding reaction snapshots from two view angles are shown in (b) pathway via **HJ-1**, and (d) pathway from **Def-4** to **Def-5**. The evolving O−O distances (unit: Å) in the moving layer are indicated. Yellow balls highlight the distinct water molecules in the moving layer, and the color scheme for others is the same as in Figure 2.

where the close-packed $(111)_c$ of ice Ic is atomically coherent with the basal plane $(0001)_h$ of ice Ih. **HJ-2** and **HJ-3** also obey **OR-1**, but with different interfaces, i.e., the $(\overline{2}11)_c//(01\overline{1}0)_h$ interface for **HJ-2** and the $(01\overline{2})_c//(1\overline{2}10)_h$ interface for **HJ-3**. **HJ-4** belongs to **OR-2**: $(001)_c//(0001)_h$; $[110]_c//[1\overline{2}10]_h$, with the interface formed between the square lattice $(001)_c$ and the basal plane $(0001)_h$. The stability of these biphase interfaces can be assessed by the interfacial energy that is directly computable using the half−half supercell approach,[33] as listed in Table 1. It shows that **HJ-1** is a remarkably stable interface, being far more stable than other interfaces with the interfacial energy being only 0.03 kJ/(mol Å^{-2}).

Indeed, **HJ-1** was observed commonly using X-ray and neutron diffraction techniques,[19,20,34] and has been named the stacking disordered ice.[19] Kuhs et al.,[10] using SEM, found that the surfaces of the as-formed "ice Ic" (at 167 K) have a high concentration of kinks on the prismatic planes, implying a large concentration of stacking disorders (**HJ-1**), and these kinks disappear only above 220 K. By contrast, the other junctions, **HJ-2** to **HJ-4**, have not been reported from experiment.

We emphasize that the stability of these junctions is related to both the lattice match (strain) and the atomic match at the biphase interface, as reflected by the interface energy. The interface area misfit ΔS can be utilized as a quick guide to understand the interface strain. As all **HJs** (**HJ-1 to HJ-3**) of **OR-1** have low lattice mismatch (<1.1% in ΔS), much smaller than that of **HJ-4** of **OR-2** (−7.78% in ΔS), this suggests that the high stability of **HJ-1** originates from both lattice and atomic coherence. In fact, only in **HJ-1** is the bulk-like H-bonding network (obeying the Bernal−Fowler rule[35]) preserved at the interface.

For the seven low-energy vacancy defects (Figure 2b), the first three structures, namely, **Def-1** to **Def-3**, are energetically

degenerate (~30 kJ/mol above Ic). They can be considered as the quasi-two-dimensional (2D) vacancy layer defects in the close-packed planes $(0001)_h$ or $(111)_c$ of the three most stable ice structures, **Ic**, **HJ-1**, and **Ih**. The vacancy defects are along the $[0\overline{1}1]_c$ or $[\overline{1}2\overline{1}0]_h$ direction with $[1 \times 1]$ periodicity along $[1\overline{1}0]_c$, forming eight-membered water rings viewed along $[1\overline{1}0]_c$ or $[2\overline{1}\overline{1}0]_h$. Apparently, the geometry of these defective structures deviates obviously from the perfect Ic or Ih with one missing H-bonding for each interface water. It should be mentioned that the Bjerrum defects (L- and D-defects) known in the literature[36] are in fact not observed in low-energy vacancy defects, as shown in Figure 2, indicating that the local geometry relaxation would remove the unfavorable H-bonding arrangements proposed by Bjerrum via simple molecular rotations.

The next three defective structures, namely, **Def-4** to **Def-6**, are higher in energy (~ 50 kJ/mol above Ic) with a one-dimensional (1D) vacancy chain along $[01\overline{1}]_c$, which leads to the five- and nine-membered water rings viewed from $[1\overline{1}0]_c$. Obviously, the first six low-energy defective structures have a common feature that vacancy defects aggregate in the close-packed $(111)_c$ or $(0001)_h$ plane along the $[01\overline{1}]_c$ or $[\overline{1}2\overline{1}0]_h$ direction. On the other hand, the remaining three defective structures, **Def-7**, **Def-8**, and **Def-9** (shown in the SI Figure S4), either contains the point vacancy defect in bulk (**Def-7**) or has the vacancy located in the open planes, i.e., $(101)_c$ for **Def-8** with five- and eight-membered rings, and $(211)_c$ for **Def-9** with five- and nine-membered rings. The **Def-7** to **Def-9** structures are far more unstable compared to the other defective structures (>58 kJ/mol above Ic).

The energetics sequence of vacancies determined from global PES indicates that the water vacancy in ice prefers to aggregate toward the close-packed plane, which may form a
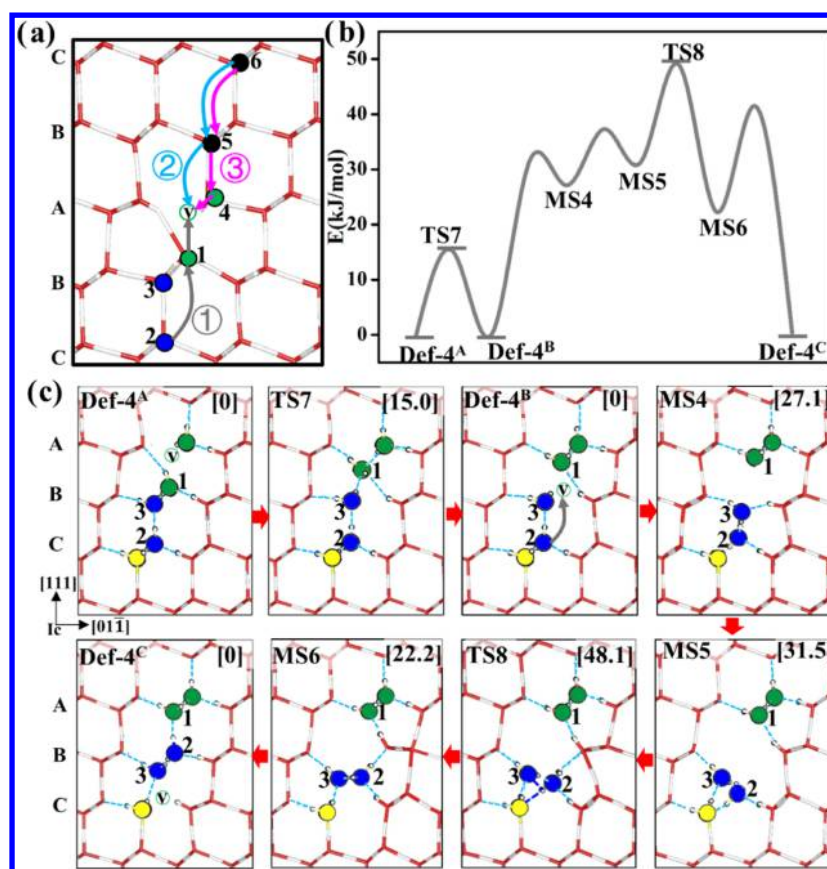
Figure 4. Vacancy diffusion in ice. (a): three possible routes for the vacancy migration pathways. (b, c): Potential energy profile (b) and reaction snapshots (c) for 1D-vacancy defect diffusion in the Ic phase (viewed from $<1\bar{1}0>_c$). The relative energetics (in kJ/mol) of the states are indicated in the top-right corner of each snapshot.

1D-vacancy chain or a 2D vacancy layer (point vacancy: 58 kJ/mol; 1D vacancy: 50 kJ/mol; 2D vacancy 30 kJ/mol). This agrees with the previous DFT findings that vacancies significantly reduce the formation energy of neighboring vacancies, thus facilitating the quasi-liquid layer formation near the vacancies.[37]

While there are many different ice vacancies, the lowest vacancy formation energies identified from global PES, ~30 kJ/mol, is consistent with the measured experimental data, 27±6 kJ/mol, from the annealing of irradiated ice.[38] This confirms that the 2D vacancy layer structures, **Def-1** to **Def-3**, are the most common vacancy defects in ice. Interestingly, for ice growth on substrates (Ru, Pt), the five-membered ice ring appears as a key feature.[39] In bulk ice, as shown here, **Def-4** to **Def-6**, having only the five-membered rings, are in fact far less stable than **Def-1** to **Def-3**.

3.2. Lowest Energy Pathways for the Ic-to-Ih Transition. Next, by using SSW reaction pathway sampling (see Section 2.1), we investigate the energy landscape for the Ic-to-Ih phase transition, which involves the identification of the lowest energy transition pathways as mediated by all different heterophase junctions and defective structures.

3.2.1. Pathway via Vacancy-Free Heterophase Junctions. The calculated overall barriers mediated by the heterophase junctions (the highest energy TS along the pathway with respect to ice Ic) are listed in Table 1, and the energetics and reaction snapshots for the lowest energy pathway via **HJ-1** are shown in Figure 3a. As shown, the lowest energy pathways via **HJ-1/2** junctions are highly preferable with the barrier below

80.8 kJ/mol, as compared to those via **HJ-3/4** junctions (>151.9 kJ/mol). This indicates that the ice phase transition also tends to grow layer-by-layer in the direction perpendicular to the basal plane following an anisotropic growth kinetics. This crystallographic direction is the same as the observed ice growth direction from liquid water,[40] suggesting that the crystallization (liquid-to-ice) and the Ic-to-Ih transition may occur consecutively in the supercooled water.

The pathway via **HJ-1** provides the most favored Ih nucleation channel among the pathways mediated by four heterophase junctions, which involves three elementary steps and two intermediate states (MS1 and MS2, Figure 3a black curve). The transition features half of a water bilayer on the $(111)_c$ plane shearing along the $<11\bar{2}>_c$ direction, as indicated by the arrows on the flat-lying water molecules in Figure 3b Ic. The other half of the bilayer remains basically unchanged with nearly the same O−O distance. It is important to observe the H-bonding change during the phase transition. We find that at TS1 and TS3, one flat-lying molecule (its two Hs forming H-bondings within the same bilayer) achieves distorted H-bondings for its two H atoms with the same neighbor O (see blue dashed line in Figure 3), breaking the Bernal−Fowler rule. This is apparently the key reason for the high barrier of the transition. After the transition, a three-layer Ih nucleus inside the Ic phase (Ih/Ic) forms (Figure 3b).

3.2.2. Pathway via Vacancy Defects. As vacancy defects are common in ice particles, it is a must to consider the phase transition pathways involving the low-energy defective structures, **Def-1**, **Def-2**, **Def-4**, and **Def-5** as the intermedi-

ates. Because of the heterogeneity of vacancies, the Ic-to-Ih transition requires multiple elementary reaction steps, including Ih nucleation, Ih growth, and the annihilation of vacancies to form perfect Ih.

For the nucleation step, we found that Ih nucleation is, surprisingly, generally facile around the vacancy defects. The reaction profiles for the lowest energy pathways with vacancies are shown in Figure 3c. The computed reaction barriers from **Def-1** (Ic only) to **Def-2** (Ih nearby vacancy) and from **Def-4** (Ic only) to **Def-5** (Ih nearby vacancy) are only 3.6 and 17.3 kJ/mol, respectively, which are substantially lower than the Ih nucleation near-vacancy-free heterophase junctions (66.3 kJ/mol). This strongly indicates that the Ih nucleation occurs exclusively near the vacancy centers.

Despite the large difference in energetics, the pathways from **Def-1** to **Def-2** or from **Def-4** to **Def-5** are in fact similar in geometrical features to the pathway via **HJ-1**, involving half of the water bilayer, where the vacancy locates to shear along the $<11\bar{2}>_c$ direction (see the arrow in Figure 3d Def-4). Being slightly different, now the other half of the water bilayer also relaxes accordingly, as reflected in the varied O−O distance. In the transition, the Bernal−Fowler rule is largely conserved for the moving water molecules, with the two H atoms of water forming two H-bondings with the neighboring Os (see the blue dashed line in TS4 of Figure 3d). This is apparently due to the local geometrical flexibility introduced by the weaker H-bonding environment, as reflected by the nine-membered water rings around vacancies, which leads to the low energy cost in water migration as required in the transition. We would emphasize that these intermediate phases along the pathway (HJ-1, Def-4, Def-5, and Def-6), despite the unconventional ring geometry, have been confirmed to be true minima, as evidenced from their phonon spectra (Figure S11 in the SI).

The subsequent Ih growth may follow two mechanisms, either Ih direct growth without the participation of vacancies, or the Ih growth after the vacancy diffusion away from the biphase junction. The former case undergoes the layer-by-layer transition by repeating the pathway via **HJ-1** and, thus, is hindered by a high barrier of 66.3 kJ/mol (this complete pathway is shown in the SI Figure S5). For the latter case, the vacancy needs to diffuse two layers away from the junction. Once finished, it would recover the defective Ic local structure (**Def-1** or **Def-4** alike) and lead to the Ih growth by two more layers. Such a diffusion is depicted in Figure 4a, where the exchange of either **6** or **2** water molecules at layer C with the vacancy at layer A will effectively make the vacancy diffuse two layers away from the original position.

Taking the diffusion of the 1D-vacancy chain in ice Ic as a model system (**Def-4**), we have studied the reaction pathway for vacancy diffusion by using the VC-DESW method. The vacancy migration in bulk ice could adopt three different routes, namely, the route $\bar{\text{i}}$ to ı in Figure 4a, which are found to have the overall reaction barriers of 48.1, 48.1, and 77.6 kJ/mol, respectively. Figure 4b,c show the energetic profile and the reaction snapshots for the lowest energy pathway, i.e., route $\bar{\text{i}}$. The energetically less favored pathway (route $\tilde{\text{I}}$) is also shown in Figure S8 in the SI. This multiple-step reaction is elaborated as follows.

The vacancy diffusion starts from water molecule **1** at layer B (Figure 4) moving along $[111]_c$ to fill the neighboring vacancy (**V**) site (**1** → **V**), which effectively changes the structure from **Def-4**^{A} to **Def-4**^{B} (the superscript indicates the vacancy position at a particular layer). This **1** → **V** step has

only a barrier of 15.0 kJ/mol. Next, water molecule **2** at the C layer takes four elementary steps to fill the vacancy at layer B, **Def-4**^{B} → MS4 → MS5 → MS6 → **Def-4**^{C}, as shown in Figure 4. In the process, water molecule **2** rotates around water molecule **3**, and the highest energy TS (TS8) appears when the two molecules, **2** and **3**, are closest in distance with one H forming two unfavorable hydrogen bondings (blue dashed line), which breaks the Bernal−Fowler rule. The overall barrier of this vacancy diffusion is 48.1 kJ/mol, much larger than that for the Ih nucleation around the vacancy (3.6∼17.3 kJ/mol), but also much lower than that for the Ih formation without the vacancy (66.3 kJ/mol).

Overall, the Ic-to-Ih phase transition mechanism is stepwise, as summarized in Scheme 1. The first step is the fast nucleation

Scheme 1. Two-Step Pathway for the Ic-to-Ih Phase Transition, Where the Presence of Vacancy Defects on the $(111)_c$ Plane Plays the Key Role^a
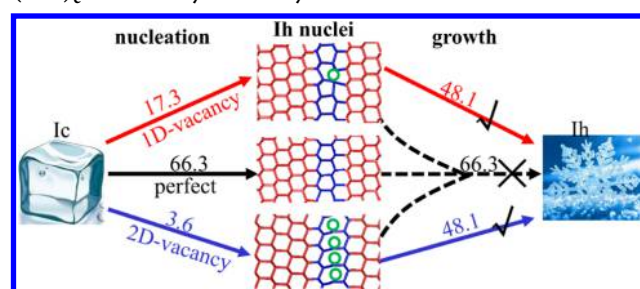
^{a}As a result, the Ih nucleus generally contains vacancies on its basal plane and the growth of the Ih phase must involve the migration of vacancy, which is the rate-determining step in the Ic-to-Ih phase transition. The key kinetic parameters, i.e., the overall reaction barrier (kJ/mol), determined from this work is indicated along the reaction direction.

step with a relatively low energy barrier (3.6−17.3 kJ/mol), which can readily occur at low temperatures, whereas the second step involves the vacancy diffusion with a high energy barrier (48.1 kJ/mol) that must occur at relatively high temperatures to allow the growth of perfect Ih. It should be emphasized that the Ic-to-Ih transition from perfect Ic has to follow the vacancy-free **HJ-1** mechanism and thus, has a much higher barrier (66.3 kJ/mol). It can be considered as kinetically hindered. Our mechanism may explain, for the first time, the measured two distinct activation energies for the transformation of the cubic crystal to the hexagonal one, 21.3 and 44.7 kJ/mol, by Sugisaki et al. using a calorimetric study.[13] Importantly, our mechanism confirms that the Ic phase persists even at a relatively high temperature because of the slow kinetics of vacancy diffusion. The Ic-to-Ih transition cannot complete at the first stage, i.e., below 190 K, in contrast to the proposal by Kuhs.[16]

The mechanism learned from here may have a profound significance on common phenomena in nature, e.g., those occurring in cirrus clouds. There are several recent studies[6,8,9] that report the possible formation of cubic ice in upper tropospheric cirrus ice clouds and its role in the observed elevated relative humidity within the clouds. The basic fact is that cubic ice, being metastable with respect to stable hexagonal ice, has a higher vapor pressure. The relative humidity within cirrus was found to be around 130% below 202 K (∼100% for pure Ih) by Gao et al.,[41] suggesting that there is a significant portion of Ic coexisting with Ih.[9] From our

results, because of the relatively high barrier of vacancy diffusion and even higher barrier of the bulk phase transition without the vacancy, the Ih nuclei (e.g., **Def-2** and **Def-5**, being defective **HJ-1**) should be kinetically stable during the phase transition, which explains the high humidity for cirrus ice.

In addition, the Ic-to-Ih phase transition follows the same $(111)_c$ and $(0001)_h$ shearing mechanism, regardless of the presence of vacancies, indicating that this crystallographic direction is the softest motion in ice and thus determines its unusual slipperiness. The creation of vacancies on surfaces, e.g., by external pressures or via introduction of impurities could lead to a weaker local H-bonding environment and thus significantly promote this ice shearing (e.g., the barrier reduction from 66.3 to 3.6 kJ/mol), which is in accordance with the concepts of the premelting of ice layers in rationalizing ice slipperiness.[42] For example, Sánchez et al.[43] have presented experimental and theoretical evidence on the surface stepwise melting of crystalline ice, showing that the utmost layer is liquid like with a much weaker H-bonding environment.

4. CONCLUSIONS

The characterization of the atomic structure of defects in solids and the clarification of their roles in material transition must rank first among goals in materials science. Although it remains to be a great challenge in experiment, we show that global optimization in combination with machine learning potential is a promising problem solver for such long-standing challenges. This work reveals the ice transformation mechanism from cubic to hexagonal phase that occurs in a wide temperature window from 150 to 240 K in nascent ice particles. A two-stage mechanism with quantitative kinetics data is now established, where the intrinsic vacancy defects play key roles to allow the stepwise solid-to-solid transition. This vacancy-controlled transition mechanism occurring at the ice basal plane interface has profound significance for understanding natural phenomena that we observe daily, ranging from humidity in clouds to unusual slipperiness of ice. The methodology and new understandings achieved may also open new routes for materials design via large-scale neural network modeling by focusing on the role of defective structures in solids.

ASSOCIATED CONTENT

Ⓢ Supporting Information

The Supporting Information is available free of charge on the ACS Publications website at DOI: 10.1021/acs.jpcc.8b08896.

More details on calculation methods; benchmark for NN against DFT calculations; other crystalline and amorphous structures of ice; 2D vacancy migration pathways (PDF)

AUTHOR INFORMATION

Corresponding Authors
*E-mail: cshang@fudan.edu.cn (C.S.).
*E-mail: zpliu@fudan.edu.cn (Z.-P.L.).

ORCID Ⓞ
Cheng Shang: 0000-0001-7486-1514
Si-Da Huang: 0000-0002-0055-1510
Zhi-Pan Liu: 0000-0002-2906-5217

REFERENCES

(1) Petrenko, V. F.; Whitworth, R. W. *Physics of Ice*; Oxford University Press: NY, 2002.

(2) Mayer, E.; Hallbrucker, A. Cubic ice from liquid water. *Nature* **1987**, *325*, 601−602.

(3) Whalley, E. Scheiner's Halo: Evidence for Ice Ic in the Atmosphere. *Science* **1981**, *211*, 389−390.

(4) Thurmer, K.; Nie, S. Formation of hexagonal and cubic ice during low-temperature growth. *Proc. Natl. Acad. Sci. U.S.A.* **2013**, *110*, 11757−11762.

(5) McMillan, J. A.; Los, S. C. Vitreous ice - irreversible transformations during warm-up. *Nature* **1965**, *206*, 806−807.

(6) Bartels-Rausch, T.; Bergeron, V.; Cartwright, J. H. E.; Escribano, R.; Finney, J. L.; Grothe, H.; Gutiérrez, P. J.; Haapala, J.; Kuhs, W. F.; Pettersson, J. B. C.; Price, S. D.; Sainz-Díaz, C. I.; Stokes, D. J.; Strazzulla, G.; Thomson, E. S.; Trinks, H.; Uras-Aytemiz, N. Ice structures, patterns, and processes: A view across the icefields. *Rev. Mod. Phys* **2012**, *84*, 885−944.

(7) Murray, B. J.; Bertram, A. K. Formation and stability of cubic ice in water droplets. *Phys. Chem. Chem. Phys.* **2006**, *8*, 186−192.

(8) Murphy, D. M. Dehydration in cold clouds is enhanced by a transition from cubic to hexagonal ice. *Geophys. Res. Lett.* **2003**, *30*, No. 2230.

(9) Murray, B. J.; Knopf, D. A.; Bertram, A. K. The formation of cubic ice under conditions relevant to Earth's atmosphere. *Nature* **2005**, *434*, 202−204.

(10) Kuhs, W. F.; Sippel, C.; Falenty, A.; Hansen, T. C. Extent and relevance of stacking disorder in "ice I(c)". *Proc. Natl. Acad. Sci. U.S.A.* **2012**, *109*, 21259−21264.

(11) Dowell, L. G.; Rinfret, A. P. Low temperature of ice as studied by X-Ray diffraction. *Nature* **1960**, *188*, 1144−1148.

(12) Handa, Y. P.; Klug, D. D.; Whalley, E. Difference in energy between cubic and hexagonal ice. *J. Chem. Phys* **1986**, *84*, 7009−7010.

(13) Sugisaki, M.; Suga, H.; Seki, S. Calorimetric Study of the Glassy State. IV. Heat Capacities of Glassy Water and Cubic Ice. *Bull. Chem. Soc. Jpn.* **1968**, *41*, 2591−2599.

(14) Kohl, I.; Mayer, E.; Hallbrucker, A. The glassy water−cubic ice system: a comparative study by X-ray diffraction and differential scanning calorimetry. *Phys. Chem. Chem. Phys.* **2000**, *2*, 1579−1586.

(15) Mayer, E.; Hallbrucker, A. Cubic ice from liquid water. *Nature* **1987**, *325*, 601−602.

(16) Kuhs, W. F.; Genov, G.; Staykova, D. K.; Hansen, T. Ice perfection and onset of anomalous preservation of gas hydrates. *Phys. Chem. Chem. Phys.* **2004**, *6*, 4917−4920.

(17) Johari, G. P. On the coexistence of cubic and hexagonal ice between 160 and 240 K. *Philos. Mag. B* **1998**, *78*, 375−383.

(18) Pirzadeh, P.; Kusalik, P. G. On understanding stacking fault formation in ice. *J. Am. Chem. Soc.* **2011**, *133*, 704−707.

(19) Malkin, T. L.; Murray, B. J.; Salzmann, C. G.; Molinero, V.; Pickering, S. J.; Whale, T. F. Stacking disorder in ice I. *Phys. Chem. Chem. Phys.* **2015**, *17*, 60−76.

(20) Hansen, T. C.; Koza, M. M.; Kuhs, W. F. Formation and annealing of cubic ice: I. Modelling of stacking faults. *J. Phys.: Condens. Matter* **2008**, *20*, No. 285104.

(21) Baker, I. Examination of Dislocations in Ice. *Cryst. Growth Des.* **2002**, *2*, 127−134.

(22) Moellmann, J.; Grimme, S. DFT-D3 Study of Some Molecular Crystals. *J. Phys. Chem. C* **2014**, *118*, 7615−7621.

(23) Huang, S. D.; Shang, C.; Zhang, X. J.; Liu, Z. P. Material discovery by combining stochastic surface walking global optimization with a neural network. *Chem. Sci.* **2017**, *8*, 6327−6337.

(24) Shang, C.; Zhang, X. J.; Liu, Z. P. Stochastic surface walking method for crystal structure and phase transition pathway prediction. *Phys. Chem. Chem. Phys.* **2014**, *16*, 17845−17856.

(25) Shang, C.; Liu, Z.-P. Stochastic Surface Walking Method for Structure Prediction and Pathway Searching. *J. Chem. Theory Comput.* **2013**, *9*, 1838−1845.

(26) Shang, C.; Liu, Z. P. Constrained Broyden Dimer Method with Bias Potential for Exploring Potential Energy Surface of Multistep Reaction Process. *J. Chem. Theory Comput.* **2012**, *8*, 2215−2222.

(27) Zhang, X. J.; Liu, Z. P. Variable-cell double-ended surface walking method for fast transition state location of solid phase transitions. *J. Chem. Theory Comput.* **2015**, *11*, 4885−4894.

(28) Kresse, G.; Furthmüller, J. Efficient iterative schemes for ab initio total-energy calculations using a plane-wave basis set. *Phys. Rev. B* **1996**, *54*, 11169−11186.

(29) Kohl, I.; Mayer, E.; Hallbrucker, A. The glassy water−cubic ice system: a comparative study by X-ray diffraction and differential scanning calorimetry. *Phys. Chem. Chem. Phys.* **2000**, *2*, 1579−1586.

(30) Russo, J.; Romano, F.; Tanaka, H. New metastable form of ice and its role in the homogeneous crystallization of water. *Nat. Mater.* **2014**, *13*, 733−739.

(31) Fennell, C. J; Gezelter, J. D. Computational Free Energy Studies of a New Ice Polymorph Which Exhibits Greater Stability than Ice Ih. *J. Chem. Theory Comput.* **2005**, *1*, 662−667.

(32) Cao, X.; Huang, Y.; Jiang, X.; Su, Y.; Zhao, J. Phase diagram of water-methane by first-principles thermodynamics: discovery of MH-IV and MH-V hydrates. *Phys. Chem. Chem. Phys.* **2017**, *19*, 15996−16002.

(33) Zhao, W. N.; Zhu, S. C.; Li, Y. F.; Liu, Z. P. Three-phase junction for modulating electron-hole migration in anatase-rutile photocatalysts. *Chem. Sci.* **2015**, *6*, 3483−3494.

(34) Malkina, T. L.; Murray, B. J.; Brukhno, A. V.; Anwar, J.; Salzmann, C. G. Salzmann Structure of ice crystallized from supercooled water. *Proc. Natl. Acad. Sci. U.S.A.* **2012**, *109*, 1041−1045.

(35) Bernal, J. D.; Fowler, R. H. A Theory of Water and Ionic Solution, with Particular Reference to Hydrogen and Hydroxyl Ions. *J. Chem. Phys.* **1933**, *1*, 515−548.

(36) Bjerrum, N. Structure and properties of ice. *Science* **1952**, *115*, 385−390.

(37) Watkins, M.; Pan, D.; Wang, E. G.; Michaelides, A.; VandeVondele, J.; Slater, B. Large variation of vacancy formation energies in the surface of crystalline ice. *Nat. Mater.* **2011**, *10*, 794−798.

(38) Mogensen, O. E.; Eldrup, M. vacancies in pure ice studied by positron annihilation techniques. *J. Glaciol.* **1978**, *21*, 85−99.

(39) Maier, S.; Lechner, B. A.; Somorjai, G. A.; Salmeron, M. Growth and Structure of the First Layers of Ice on Ru(0001) and Pt(111). *J. Am. Chem. Soc.* **2016**, *138*, 3145−3151.

(40) Rozmanov, D.; Kusalik, P. G. Anisotropy in the crystal growth of hexagonal ice, I(h). *J. Chem. Phys.* **2012**, *137*, No. 094702.

(41) Gao, R. S.; Popp, P. J.; Fahey, D. W.; Marcy, T. P.; Herman, R. L.; Weinstock, E. M.; Baumgardner, D. G.; Garrett, T. J.; Rosenlof, K. H.; Thompson, T. L.; Bui, P. T.; Ridley, B. A.; Wofsy, S. C.; Toon, O. B.; Tolbert, M. A.; Karcher, B.; Peter, T.; Hudson, P. K.; Weinheimer, A. J.; Heymsfield, A. J. Evidence that nitric acid increases relative humidity in low-temperature cirrus clouds. *Science* **2004**, *303*, 516−520.

(42) Li, Y.; Somorjai, G. A. Surface Premelting of Ice. *J. Phys. Chem. C* **2007**, *111*, 9632−9637.

(43) Sánchez, M. A.; Kling, T.; Ishiyama, T.; van Zadel, M. J.; Bisson, P. J.; Mezger, M.; Jochum, M. N.; Cyran, J. D.; Smit, W. J.; Bakker, H. J.; Shultz, M. J.; Morita, A.; Donadio, D.; Nagata, Y.; Bonn, M.; Backus, E. H. Experimental and theoretical evidence for bilayer-by-bilayer surface melting of crystalline ice. *Proc. Natl. Acad. Sci. U.S.A.* **2017**, *114*, 227−232.